

High speed, wide velocity dynamic range Doppler optical coherence tomography (Part IV): split spectrum processing in rotary catheter probes

Barry Vuong,¹ Anthony M.D. Lee,² Timothy W.H. Luk,¹ Cuiru Sun,¹
Stephen Lam,² Pierre Lane,² and Victor X.D. Yang^{1,3,4,*}

¹ Biophotonics and Bioengineering Laboratory, Dept. Electrical and Computer Engineering,
Ryerson University, Toronto, ON, Canada

² Department of Integrative Oncology - Cancer Imaging Unit, British Columbia Cancer
Research Centre, Vancouver, BC, Canada

³ Division of Neurosurgery, Sunnybrook Health Sciences Centre, Toronto, ON, Canada

⁴ Division of Neurosurgery, Faculty of Medicine, University of Toronto, ON, Canada

*yangv@ee.ryerson.ca

Abstract: We report a technique for blood flow detection using split spectrum Doppler optical coherence tomography (ssDOCT) that shows improved sensitivity over existing Doppler OCT methods. In ssDOCT, the Doppler signal is averaged over multiple sub-bands of the interferogram, increasing the SNR of the Doppler signal. We explore the parameterization of this technique in terms of number of sub-band windows, width and overlap of the windows, and their effect on the Doppler signal to noise in a flow phantom. Compared to conventional DOCT, ssDOCT processing has increased flow sensitivity. We demonstrate the effectiveness of ssDOCT *in-vivo* for intravascular flow detection within a porcine carotid artery and for microvascular vessel detection in human pulmonary imaging, using rotary catheter probes. To our knowledge, this is the first report of visualizing *in-vivo* Doppler flow patterns adjacent to stent struts in the carotid artery.

© 2014 Optical Society of America

OCIS codes: (170.4500) Optical Coherence Tomography; (170.3880) Medical and biological imaging; (120.5050) Phase measurement.

References and links

1. G. Tearney, S. Boppart, B. Bouma, M. Brezinski, N. Weissman, J. Southern, and J. Fujimoto, "Scanning single-mode fiber optic catheter-endoscope for optical coherence tomography," *Opt. Lett.* **21**, 543–545 (1996).
2. K. H. Cheng, C. Sun, B. Vuong, K. K. Lee, A. Mariampillai, T. R. Marotta, J. Spears, W. J. Montanera, P. R. Herman, T.-R. Kiehl *et al.*, "Endovascular optical coherence tomography intensity kurtosis: visualization of vasa vasorum in porcine carotid artery," *Biomed. Opt. Express* **3**, 388–399 (2012).
3. B. J. Vakoc, M. Shishko, S. H. Yun, W.-Y. Oh, M. J. Suter, A. E. Desjardins, J. A. Evans, N. S. Nishioka, G. J. Tearney, and B. E. Bouma, "Comprehensive esophageal microscopy by using optical frequency-domain imaging (with video)," *Gastrointestinal endoscopy* **65**, 898–905 (2007).
4. A. M. Lee, K. Ohtani, C. MacAulay, A. McWilliams, T. Shaipanich, V. X. Yang, S. Lam, and P. Lane, "In vivo lung microvasculature visualized in three dimensions using fiber-optic color doppler optical coherence tomography," *J. Biomed. Opt.* **18**, 050501 (2013).

5. C. Sun, F. Nolte, K. H. Cheng, B. Vuong, K. K. Lee, B. A. Standish, B. Courtney, T. R. Marotta, A. Mariampillai, and V. X. Yang, "In vivo feasibility of endovascular doppler optical coherence tomography," *Biomed. Opt. Express* **3**, 2600–2610 (2012).
6. X. Li, T. H. Ko, and J. G. Fujimoto, "Intraluminal fiber-optic doppler imaging catheter for structural and functional optical coherence tomography," *Opt. Lett.* **26**, 1906–1908 (2001).
7. M. J. McCarthy, I. M. Loftus, M. M. Thompson, L. Jones, N. J. London, P. R. Bell, A. R. Naylor, and N. P. Brindle, "Angiogenesis and the atherosclerotic carotid plaque: an association between symptomatology and plaque morphology," *J. Vascular Surgery* **30**, 261–268 (1999).
8. N. F. Voelkel, I. S. Douglas, and M. Nicolls, "Angiogenesis in chronic lung disease," *CHEST Journal* **131**, 874–879 (2007).
9. A. Yuan, D.-B. Chang, C.-J. Yu, S. Kuo, K. Luh, and P. Yang, "Color doppler sonography of benign and malignant pulmonary masses," *AJR. American journal of roentgenology* **163**, 545–549 (1994).
10. B. Vakoc, S. Yun, J. De Boer, G. Tearney, and B. Bouma, "Phase-resolved optical frequency domain imaging," *Opt. Express* **13**, 5483–5493 (2005).
11. B. Braaf, K. A. Vermeer, V. A. D. Sicam, E. van Zeeburg, J. C. van Meurs, and J. F. de Boer, "Phase-stabilized optical frequency domain imaging at 1- μm for the measurement of blood flow in the human choroid," *Opt. Express* **19**, 20886–20903 (2011).
12. Y.-J. Hong, S. Makita, F. Jaillon, M. J. Ju, E. J. Min, B. H. Lee, M. Itoh, M. Miura, and Y. Yasuno, "High-penetration swept source doppler optical coherence angiography by fully numerical phase stabilization," *Opt. Express* **20**, 2740–2760 (2012).
13. B. White, M. Pierce, N. Nassif, B. Cense, B. Park, G. Tearney, B. Bouma, T. Chen, and J. de Boer, "In vivo dynamic human retinal blood flow imaging using ultra-high-speed spectral domain optical coherence tomography," *Opt. Express* **11**, 3490–3497 (2003).
14. G. van Soest, J. G. Bosch, and A. F. van der Steen, "Azimuthal registration of image sequences affected by nonuniform rotation distortion," *IEEE Trans. Info.Tech. Biomed.* **12**, 348–355 (2008).
15. V. X.D. Yang, M. L. Gordon, B. Qi, J. Pekar, S. Lo, E. Seng-Yue, A. Mok, B. C. Wilson, and A. I. Vitkin, "High speed, wide velocity dynamic range doppler optical coherence tomography (part i): System design, signal processing, and performance," *Opt. Express* **11**, 794–809 (2003).
16. H. Ren and X. Li, "Clutter rejection filters for optical doppler tomography," *Opt. Express* **14**, 6103–6112 (2006).
17. D. W. Cadotte, A. Mariampillai, A. Cadotte, K. K. Lee, T.-R. Kiehl, B. C. Wilson, M. G. Fehlings, and V. X. Yang, "Speckle variance optical coherence tomography of the rodent spinal cord: in vivo feasibility," *Biomed. Opt. Express* **3**, 911–919 (2012).
18. V. X.D. Yang, M. L. Gordon, E. Seng-Yue, S. Lo, B. Qi, J. Pekar, A. Mok, B. C. Wilson, and A. I. Vitkin, "High speed, wide velocity dynamic range doppler optical coherence tomography (part ii): Imaging in vivo cardiac dynamics of xenopus laevis," *Opt. Express* **11**, 1650–1658 (2003).
19. J. A. Jensen, *Estimation of blood velocities using ultrasound: a signal processing approach* (Cambridge University Press, 1996).
20. R. S. Cobbold, *Foundations of biomedical ultrasound* (Oxford University Press on Demand, 2007).
21. S. Yun, G. Tearney, J. De Boer, and B. Bouma, "Motion artifacts in optical coherence tomography with frequency-domain ranging," *Opt. Express* **12**, 2977–2998 (2004).
22. E. W. Beasley and H. R. Ward, "A quantitative analysis of sea clutter decorrelation with frequency agility," *Aerospace and Electronic Systems, IEEE Transactions on* pp. 468–473 (1968).
23. P. Karpur and O. J. Canelones, "Split spectrum processing: a new filtering approach for improved signal-to-noise ratio enhancement of ultrasonic signals," *Ultrasonics* **30**, 351–357 (1992).
24. G. van Soest, M. Villiger, E. Regar, G. J. Tearney, B. E. Bouma, and A. F. van der Steen, "Frequency domain multiplexing for speckle reduction in optical coherence tomography," *J. Biomed. Opt.* **17**, 0760181–0760187 (2012).
25. Y. Jia, O. Tan, J. Tokayer, B. Potsaid, Y. Wang, J. J. Liu, M. F. Kraus, H. Subhash, J. G. Fujimoto, J. Hornegger, and D. Haug, "Split-spectrum amplitude-decorrelation angiography with optical coherence tomography," *Opt. Express* **20**, 4710–4725 (2012).
26. M. Wojtkowski, A. Kowalczyk, R. Leitgeb, and A. Fercher, "Full range complex spectral optical coherence tomography technique in eye imaging," *Opt. Lett.* **27**, 1415–1417 (2002).
27. V. X. Yang, M. Gordon, S.-j. Tang, N. Marcon, G. Gardiner, B. Qi, S. Bisland, E. Seng-Yue, S. Lo, J. Pekar *et al.*, "High speed, wide velocity dynamic range doppler optical coherence tomography (part iii): in vivo endoscopic imaging of blood flow in the rat and human gastrointestinal tracts," *Opt. Express* **11**, 2416–2424 (2003).
28. K. K. Lee, A. Mariampillai, J. X. Yu, D. W. Cadotte, B. C. Wilson, B. A. Standish, and V. X. Yang, "Real-time speckle variance swept-source optical coherence tomography using a graphics processing unit," *Biomedical Opt. Express* **3**, 1557–1564 (2012).
29. S. Makita, F. Jaillon, I. Jahan, and Y. Yasuno, "Noise statistics of phase-resolved optical coherence tomography imaging: single-and dual-beam-scan doppler optical coherence tomography," *Opt. Express* **22**, 4830–4848 (2014).
30. S. Yazdanfar, C. Yang, M. Sarunic, and J. Izatt, "Frequency estimation precision in doppler optical coherence

- tomography using the cramer-rao lower bound,” *Opt. Express* **13**, 410–416 (2005).
31. B. Park, M. C. Pierce, B. Cense, S.-H. Yun, M. Mujat, G. Tearney, B. Bouma, and J. de Boer, “Real-time fiber-based multi-functional spectral-domain optical coherence tomography at 1.3 μm ,” *Opt. Express* **13**, 3931–3944 (2005).
 32. V. X. Yang, M. L. Gordon, A. Mok, Y. Zhao, Z. Chen, R. S. Cobbold, B. C. Wilson, and I. Alex Vitkin, “Improved phase-resolved optical doppler tomography using the kasai velocity estimator and histogram segmentation,” *Opt. Commun.* **208**, 209–214 (2002).
 33. D. Rockwell, “Vortex-body interactions,” *Annual review of fluid mechanics* **30**, 199–229 (1998).
 34. J. E. Moore Jr and J. L. Berry, “Fluid and solid mechanical implications of vascular stenting,” *Annals of biomedical engineering* **30**, 498–508 (2002).
-

1. Introduction

Optical coherence tomography (OCT) imaging using optical fiber-based rotary catheter probes provides 2D and 3D visualization of microstructures in tissue and has shown initial success in the cardiovascular [1, 2], gastroesophageal [3], and pulmonary systems [4]. These clinical studies suggest that rotary catheters provide useful *in-vivo* diagnostic information based on the structural morphology in the tissue. Doppler OCT, an extension of OCT, has been used with rotary catheter probes to visualize and quantify flow [4–6]. The ability to measure flow and microvascular architectures may provide insight into the detection and progression of various diseases.

In a normal human carotid artery, the peak systolic velocities can be ≈ 100 cm/s, but this velocity can increase up to ≈ 230 cm/s as the degree of stenosis becomes more severe [7]. As a result, the detection of vascular remodeling may lead to appropriate treatment planning and prevent future adverse events. In addition, imaging analysis of flow velocity distribution within the vessel lumen can potentially provide important diagnostic information about vascular pathology, such as atherosclerotic plaque induced stenosis, as well as therapeutic monitoring before and after stenting procedures. Endovascular DOCT, however, requires carefully controlled saline flushing [5], which demands Doppler signal detection from relatively low signal to noise regions as affected by the saline.

Vascular remodeling is also a key process of vascular development in pulmonary diseases [8]. Large malignant pulmonary masses (1 to 8 cm) have been observed to have a peak systolic velocity of 0.17 ± 0.07 m/s using color Doppler ultrasound [9]. Smaller blood vessels in the airways are difficult to visualize using conventional imaging modalities. Recent DOCT has shown ≈ 2 mm/s flow velocities within a blood vessel along the human airways [4]. Further DOCT imaging studies of patients with lung malignancy may demonstrate DOCT as an effective tool to quantify the effects of treatment therapies.

High phase stability of the OCT laser source and its wavelength sweeping synchronization (swept source OCT) with the data acquisition, is required for Doppler imaging. This can be achieved through well-designed laser sources or phase stabilization schemes. Current phase stabilizing schemes consist of measuring the phase of a stationary reflective element and compensating for the unstable phase numerically [10, 11]. Phase stabilization has also been demonstrated without additional hardware or optical components [12]. In terms of spectrometer-based OCT, the phase stability is high relative to swept source OCT [13]. However spectral domain OCT suffers from fringe washout, limiting the ability to detect fast moving structures.

In rotary catheter probes, Doppler signals are degraded by mechanical vibrations induced by the rotation of the optical components, as well as the movement of the catheter sheath and variations in rotational speed, resulting in non-uniform rotational distortion (NURD) [14]. Currently, the techniques used to suppress these artefacts consist of careful selection of both the Kasai autocorrelation window and relatively phase stable reference regions in order to remove bulk motion [15]. This intra-frame technique is less sensitive to bulk motion from the probe and

tissue [4].

Improvement of noisy Doppler signal can also be achieved by averaging over multiple frames of the same location. This inter-frame method is not commonly utilized for a number of reasons. First, Doppler signal can still be influenced by noise even after conventional spatial averaging due to the stationary scatterers that coexist with the moving scatterers of the coherent sampling volume in the catheter. This would limit the accuracy and sensitivity in the flow velocity estimation, particularly with slow flow velocities seen in capillaries and small blood vessels [16]. Second, *in-vivo* imaging of multiple scans at the exact same location is not practical as each rotational scan can be influenced by breathing [17], blood pulsation [18], NURD [14], or other environmental motion.

In ultrasound, the transducer bandwidth plays a role in the standard deviation of velocity estimation. Jensen [19] derived that the narrowing of the frequency spectrum results in a longer-range gate and higher velocity resolution. Furthermore, longer-range gate deposits high amounts of power leading to higher SNR [20]. This derivation is based on two radio frequency (RF) sampled square wave envelopes, which does not apply to OCT. However, the basis of the variance of Doppler shift can be applied to OCT and is shown by the following [19]:

$$\sigma_D^2 \approx \frac{2}{T_{prf}^2} \left(1 - \frac{|R(T_{prf})|}{R(0)} \right) \quad (1)$$

where T_{prf} is the time of the pulse repetition frequency, $|R(T_{prf})|$ is determined by the auto-correlation function of the envelope of the pulse, $R(0)$ is the power of the received signal, and $R_{gg}(T_{prf})$ denotes the value found from correlating two measured RF lines.

The time displacement between two RF lines is

$$t_s = \frac{2v_z}{c} T_{prf} \quad (2)$$

where c is the speed of sound and v_z the axial velocity of the sample.

In OCT, the axial displacement between two adjacent A-lines is

$$\Delta z = v_z T = \frac{v_z}{f_a} \quad (3)$$

where f_a is the axial scan rate of the OCT. When the velocity increases, the Doppler shift estimation error increases [15] as Δz becomes increasingly larger in comparison to the coherence gate (l_c) of a time-domain OCT system.

In the past decade, the OCT research field has advanced from time-domain to frequency domain OCT, including swept source OCT. Yun et al. [21] (Eq. (18)) modelled the depth profile of a swept source OCT in terms of depth, Z , to be:

$$F(Z) \approx \gamma P_o \int \int \int dx dy dz r(x, y, z) g(x - x_b, y - y_b) \exp(-i2k_o Z) \int_{-\infty}^{\infty} \exp(-4 \ln 2 \frac{k^2}{(2k_1 T \sigma)^2}) \exp(i(2k_o + k)(Z - z_o - \frac{v_z}{2k_1} k)) dk \quad (4)$$

$$F(Z) \propto \gamma P_o \int \int \int dx dy dz r(x, y, z) \exp(-i2k_o z_o) \exp(-4 \ln 2 \frac{(x-x_b)^2}{w_o^2}) \exp(-4 \ln 2 \frac{(y-y_b)^2}{w_o^2}) \exp(-4 \ln 2 \frac{(Z - [z_o + (k_o/k_1) T \Delta z])^2}{\delta z_o^2 (1 + 4 \sigma^2 \Delta z^2 / \delta z_o^2)}) \quad (5)$$

where γ is the photon-to-electron conversion efficiency, $P_o = \sqrt{P_r(t)P_s(t)}$, $P_r(t)$ is the optical power returned from the reference arm, $P_s(t)$ the optical power turned from the sample arm (sample at 100% reflection), $r(x, y, z)$ denote the complex-valued backscattering coefficient, $g(x, y, z)$ represents the intensity profile of the probe beam in the sample arm, (x_b, y_b, z_b) is

the coordinates of the probe beam at zero path length difference of the interferometer, w_o is the beam waist, $\sigma k_1 T$ is the full width half maximum (FWHM) tuning range in wavenumber, $k(t) = k_o + k_1 t$ is the output wavenumber that is tuned linearly in time, and $\delta z_o = \frac{4 \ln(2)}{k_1 T \sigma}$ FWHM axial resolution, equivalent to l_c , the coherence gate in a time domain system.

From Eq. (5), we let upslon be the coherent sum of all backscattered light from a coherence volume that has a size w_0 by w_0

$$\Upsilon = \gamma P_o \int \int \int dx dy dz r(x, y, z) \exp(-i2k_o z_o) \exp(-4 \ln 2 \frac{(x-x_b)^2}{w_o^2}) \exp(-4 \ln 2 \frac{(y-y_b)^2}{w_o^2}) \quad (6)$$

then Eq. (5) is simplified to,

$$F(Z) \propto \Upsilon \exp(-4 \ln 2 \frac{(Z - [z_o + (k_o/k_1 T) \Delta z])^2}{\delta z_o^2 (1 + 4 \sigma^2 \Delta z^2 / \delta z_o^2)}) \quad (7)$$

where

$$z' = z_o + z_D \quad (8)$$

and [21]

$$z_D = \frac{k_o}{k_1 T} \Delta z = \frac{\pi \sigma}{2 \ln 2} \frac{\delta z_o}{\lambda} \Delta z \quad (9)$$

Therefore Eq. (7) becomes

$$F(Z) \propto \Upsilon \exp(-4 \ln 2 \frac{(Z - z')^2}{\delta z_o^2 (1 + 4 \sigma^2 \Delta z^2 / \delta z_o^2)}) \quad (10)$$

When measuring the Doppler shift between two adjacent A-line scans, the autocorrelation of the depth profiles is calculated. From the Wiener-Khinchin theorem, the autocorrelation is the following:

$$\overline{F(Z)} \cdot F(Z) = R_{gg}(\tau) = \int_{-\infty}^{\infty} f(\tau) f(\tau + t) d\tau \quad (11)$$

where $F(Z)$ is the Fourier transform of $f(k)$ and $\overline{F(Z)}$ is the complex conjugate

If the initial A-line scan is $F_{T_o}(Z)$ and the adjacent A-line scan is F_{T_1} then,

$$F_{T_o}(Z) \propto \Upsilon \exp(-4 \ln 2 \frac{(Z - z'_{T_o})^2}{\delta z_o^2 (1 + 4 \sigma^2 \Delta z^2 / \delta z_o^2)}) \quad (12)$$

and

$$F_{T_1}(Z) \propto \Upsilon \exp(-4 \ln 2 \frac{(Z - z'_{T_1})^2}{\delta z_o^2 (1 + 4 \sigma^2 \Delta z^2 / \delta z_o^2)}) \quad (13)$$

The autocorrelation between the two adjacent lines is

$$\overline{F_{T_1}(Z)} \cdot F_{T_o}(Z) = \overline{\Upsilon} \exp(4 \ln 2 \frac{(Z - z'_{T_1})^2}{\delta z_o^2 (1 + 4 \sigma^2 \Delta z^2 / \delta z_o^2)}) \cdot \Upsilon \exp(-4 \ln 2 \frac{(Z - z'_{T_o})^2}{\delta z_o^2 (1 + 4 \sigma^2 \Delta z^2 / \delta z_o^2)}) \quad (14)$$

$$= |\Upsilon|^2 \exp(-4 \ln 2 \frac{2Z \Delta z'}{\delta z_o^2 (1 + 4 \sigma^2 \Delta z^2 / \delta z_o^2)}) \exp(4 \ln 2 \frac{z'_{T_1}{}^2 - z'_{T_o}{}^2}{\delta z_o^2 (1 + 4 \sigma^2 \Delta z^2 / \delta z_o^2)}) \quad (15)$$

where $\Delta z'$ is difference in the depth of a moving scatterer and is related to its velocity. This equation determines OCT equivalent to $R_{gg}(\tau)$ in Eq 1. $R_{gg}(T_{prf})$ denotes the value evaluated from correlating the RF lines. In OCT the value from the correlating the two depth measurements is $R_{gg}(\Delta z')$ and $\Delta z' = z'_{T_1} - z'_{T_0} = v_z T$. As a result, Eq. (15) becomes

$$R_{gg}(\Delta z') = |\Upsilon|^2 \exp\left(-4\ln 2 \frac{2\Delta z'^2}{\delta z_0^2(1 + 4\sigma^2 \Delta z'^2 / \delta z_0^2)}\right) \exp\left(4\ln 2 \frac{z_{T_1}^2 - z_{T_0}^2}{\delta z_0^2(1 + 4\sigma^2 \Delta z'^2 / \delta z_0^2)}\right) \quad (16)$$

The power of the received signal, $R(0)$ is

$$R_{gg}(0) = |\Upsilon|^2 \exp\left(4\ln 2 \frac{z_{T_1}^2 - z_{T_0}^2}{\delta z_0^2(1 + 4\sigma^2 \Delta z'^2 / \delta z_0^2)}\right) \quad (17)$$

Inserting Eq. (16) and Eq. (17) into Eq. (1) yields

$$\sigma_D^2 \approx 2f_a^2 \left(1 - \frac{|R(\Delta z')|}{R(0)}\right) \quad (18)$$

$$\approx 2f_a^2 \left(1 - \exp\left(-4\ln 2 \frac{2\Delta z'^2}{\delta z_0^2(1 + 4\sigma^2 \Delta z'^2 / \delta z_0^2)}\right)\right) \quad (19)$$

$$\approx 2f_a^2 \left(1 - \exp\left(-4\ln 2 \frac{2(v_z T)^2}{\delta z_0^2(1 + 4\sigma^2 (v_z T)^2 / \delta z_0^2)}\right)\right) \quad (20)$$

The standard deviation of the Doppler shift estimate is then

$$\sigma_D \approx f_a \sqrt{2 \left(1 - \exp\left(-4\ln 2 \frac{2(v_z T)^2}{\delta z_0^2(1 + 4\sigma^2 (v_z T)^2 / \delta z_0^2)}\right)\right)} \quad (21)$$

This is applicable to both time domain and swept source OCT systems. In our initial companion paper [15], velocity variance measurements were obtained at various set flow velocities. These measurements were fitted to an inverted Gaussian curve, but no theoretical basis were developed. Eq. (21) demonstrates a relationship between velocity and standard deviation of the Doppler shift. The result of this equation can be seen in Figure 1, where the coherence length of the system was accounted for ($l_c = 12\mu m$). The predicted standard deviation demonstrates good agreement with measured data points. If the coherence length was lengthened by using only a fraction of the available bandwidth (FBW), then the standard deviation of the Doppler shift will decrease as per Eq. (21). This is illustrated in two scenarios of FBW at 50% and 25% in Figure 1, with decreasing phase noise.

Therefore to further suppress the Doppler artefacts on a single acquired frame, we propose a signal processing technique known as split spectrum processing (SSP). SSP was first introduced in radar to resolve concealed targets in randomly distributed reflection, known as clutter [22]. Subsequent application of this method was applied to ultrasound as a frequency agility technique for flaw detection in materials without the typical loss of spatial resolution associated with axial averaging. This was achieved by decomposing the received wideband ultrasound signal into a narrowband ensemble, producing a higher signal to noise ratio (SNR) than conventional temporal averaging [23]. Initial applications of SSP in OCT have been utilized on the resultant amplitude image to reduce speckle [24] and increase amplitude-decorrelation SNR for blood vessel detection [25]. Various types of noise sources can influence the SNR of an OCT signal. One particular source of noise is incoherent random noise, often associated with electronic instruments. These types of noise can often be removed by conventional temporal

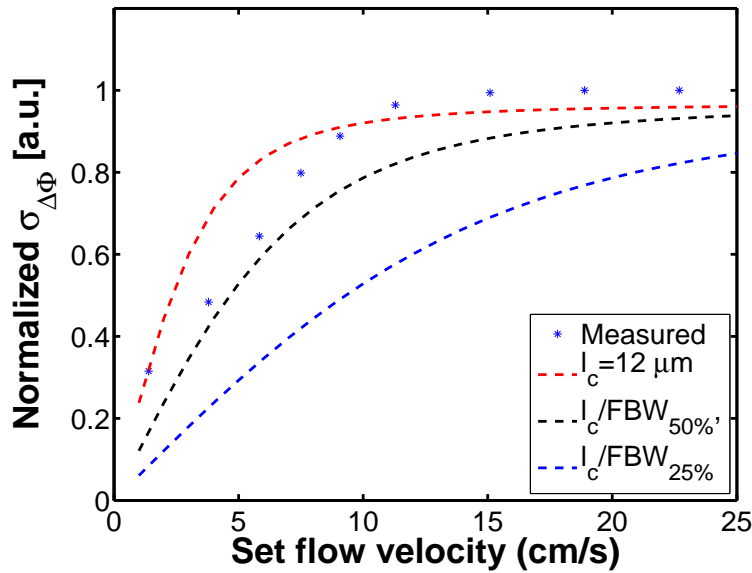


Fig. 1. Normalized standard deviation of phase shift ($\sigma_{\Delta\Phi}$) versus flow velocity. The result of Eq. (21) with the coherence length (l_c) of the system from [15] was plotted. Coherence length was increased by a factor of 2 and 4 (spectral bandwidth decreases to 50% and 25%) via fractional bandwidth (FBW) and the respective phase noise ($\sigma_{\Delta\Phi}$) of were plotted as well.

averaging. However, coherent noise sources produced by mutual interference of all elementary waves scattered within the sample are invariable with time [26]. As a result, more complex techniques are required to reduce noise. In this paper, we incorporate SSP in the evaluation of the phase from the OCT image to determine blood flow velocities. This split spectrum Doppler OCT (ssDOCT) technique differs from the conventional spatial averaging as the frequency domain of the interferogram is split into multiple narrow window bands. Various lengths of window bands, the number of bands and the window overlap were investigated. We demonstrate that this novel ssDOCT technique can provide a more sensitive velocity estimation and expands upon the conventional method outlined in our companion papers [15, 18, 27].

2. Materials and Methods

2.1. Doppler Optical Coherence Tomography rotary catheter systems

Two different DOCT rotary catheter systems were utilized in this study. A brief description follows; more detailed descriptions of the DOCT rotary catheter system have been previously presented [4,5]. In the phantom and *in-vivo* porcine carotid artery studies, a commercial clinical OCT system, the C7-XR (LightLab Imaging, St. Jude Medical Inc., USA), was connected to a personal computer equipped with a high speed data acquisition card (ATS9350, AlazarTech, Canada) and graphics processing unit (GeForce GTX 460, 1GB, NVIDIA, USA). The k-clock, A-scan trigger, and raw OCT fringe signals from the C7-XR system were coupled to the data acquisition card and processed using custom graphical accelerated software [28]. The swept source laser in the C7-XR had a bandwidth of 110nm centered at 1310nm and an A-line rate of 50.4 kHz. The imaging catheter used in this study was the C7 Dragonfly (LightLab Imaging, St. Jude Medical Inc., USA), which has a spot size of 25 μm and a working distance from the

edge of the catheter of approximately 1.5 mm, with 18.5 mW of power on the sample. OCT images were acquired at 2520 A-lines per frame at 1200 rpm. Using these imaging parameters, the Doppler signal had been shown to be satisfactory [5] after a significant amount of averaging was applied.

For human airway imaging, a fiber-based Mach-Zehnder OCT interferometer and a 50.4kHz swept source laser (SSOCT-1310, Axsun Technologies Inc., USA) system were used with a measured best system phase stability of $\Delta\phi = 0.01$ rad by a common path benchmark. A custom-built rotary-pullback drive using a fiber optical rotary junction (MJP-SAPB, Princetel Inc., USA) coupled the swept source laser (output power ≈ 15 mW) and the Dragonfly catheter. Polarization diverse interference signals were detected using a pair of detectors (PDB420C, Thorlabs Inc., USA) and a high speed digitizer (ATS9350, AlazarTech, Canada) [4].

2.2. Split Spectrum Doppler Optical Coherence Tomography

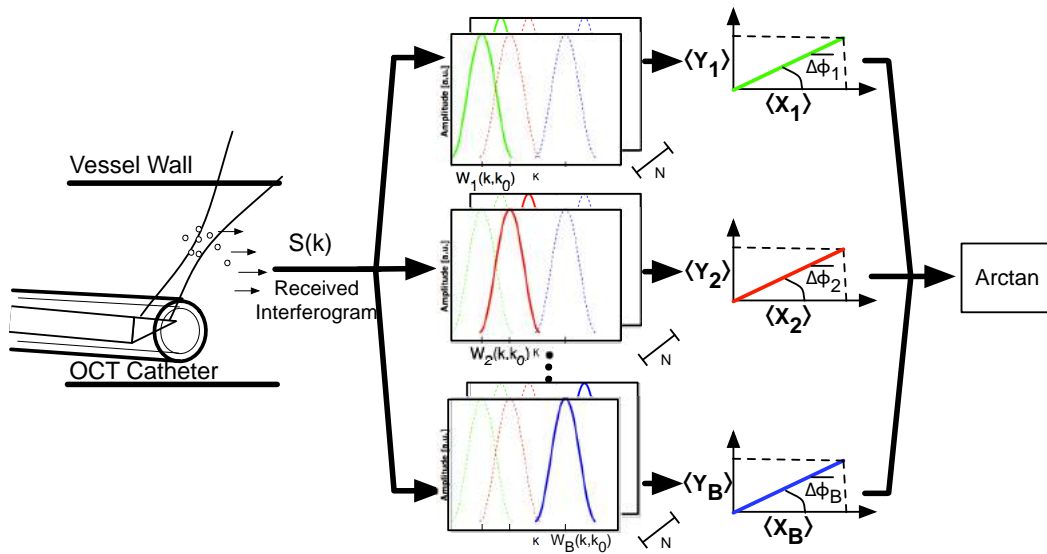


Fig. 2. Data acquisition and processing scheme. The OCT rotary catheter was inserted into a vessel and images were acquired during blood flow. Multiple narrow window bands with different center frequencies were multiplied with the interferogram. These windowed spectra were stored into the corresponding windowed band frame and the mean phase shift was calculated by evaluating the phase difference between axial scans within the frame (Eq. (23)).

Figure 2 depicts the ssDOCT algorithm, where window functions $W_b(k, k_0)$ splits the interferogram $S(k)$ into multiple bands. These apodization bands have a continuous profile (no clipping at the border of the available range), are overlapped and span the entire spectrum of the interferogram. This reduces any artefacts and/or loss of information in the OCT image. The center wavenumber of these bands is denoted as k_0 and are equally spaced across the entire interferogram. Each band is zero-padded to the length of the original record length and the inverse fast Fourier transformed (F^{-1}) was evaluated, resulting in a complex OCT signal (S) for each band (b) with respect to the optical path difference (z) between the sample and reference arms.

$$S_b(z) = F^{-1}[W_b(k, k_0)S(k)] = I_b(z) + jQ_b(z) \quad (22)$$

The in-phase (I_b) and quadrature (Q_b) signals from each of these bands generate their own unique mean phase ($\overline{\Delta\phi}$) realization, which is then evaluated by the arctan of the Kasai autocorrelation equation. The average phase shift vectors are denoted as $\langle X_b \rangle$ and $\langle Y_b \rangle$ for each window band and are extensions of the single (complete) spectrum Kasai autocorrelation equation [15]:

$$f_D = \frac{f_a}{2\pi} \arctan \left\{ \frac{\frac{1}{BM(N-1)} \sum_{b=1}^B \sum_{m=1}^M \sum_{n=1}^{N-1} (I_{b,m,n+1} Q_{b,m,n} - Q_{b,m,n+1} I_{b,m,n})}{\frac{1}{BM(N-1)} \sum_{b=1}^B \sum_{m=1}^M \sum_{n=1}^{N-1} (Q_{b,m,n+1} Q_{b,m,n} + I_{b,m,n+1} I_{b,m,n})} \right\} \\ = \frac{f_a}{2\pi} \arctan \left\{ \frac{\frac{1}{B} \sum_{b=1}^B \langle X_b \rangle}{\frac{1}{B} \sum_{b=1}^B \langle Y_b \rangle} \right\} \quad (23)$$

where f_D is the Doppler frequency shift, f_a is the A-line rate. The Kasai autocorrelation equation is performed on a window size of M in the axial direction, and by N in the transverse direction.

In order to understand the effects of ssDOCT, several parameters such as the number of window bands, the bandwidth of each band, and the amount of overlap between the window bands were investigated. In this study, we quantified the effects of the aforementioned ssDOCT parameters using a Hamming apodization window chosen for its low side lobe amplitude.

For structural imaging, the amplitude of the OCT signal from each band was compounded. Spatial averaging in the lateral direction was performed to improve the SNR. Any given pixel in the structural image was resolved by the following equation:

$$\langle S^2 \rangle = \frac{1}{BMN} \sum_{b=1}^B \sum_{m=1}^M \sum_{n=1}^N [I_{b,m,n}^2 + Q_{b,m,n}^2] \quad (24)$$

2.3. Background noise and slow flow phantom analysis

A gelatin phantom with titanium dioxide as the scatterer was constructed and imaged without any flowing fluid as a baseline measurement for bulk motion induced by the rotating catheter. A series of 20 frames were acquired at one site. In each frame, the same high SNR and low SNR region positions were selected. The intraframe standard deviation of the phase shift ($\Delta\phi$) was considered the Doppler phase noise floor. Large ensemble lengths were then observed by holding the rotary probe stationary (M-mode). Once the Doppler phase noise floor was established, optimal ssDOCT parameters were selected and used on slow flow phantom and *in-vivo* imaging. The slow flow velocity measurements were acquired by the DOCT rotary catheter using a calibrated infusion pump coupled to a plastic tube (inner diameter of approximately 3 mm). A diluted mixture of porcine blood (1.5% blood in saline) was pumped at a peak velocity of 2.5mm/s, calculated based on ANSYS simulation (V13.0, ANSYS Inc., USA) using typical catheter position geometry.

2.4. In-vivo imaging protocol and data analysis

In this work, *in-vivo* OCT imaging studies were conducted 1) in a porcine carotid artery, and 2) in human airways using the C7 dragonfly catheters. Animal and human protocols were approved by the Animal Care Committee at St. Michael's Hospital (Toronto, Canada) and the Research Ethics Board of the University of British Columbia & the British Columbia Cancer Agency (Vancouver, Canada), respectively. All human subjects gave written and informed consent. Analysis was implemented using MATLAB R2012b (Mathworks, USA) and computed on an Intel Core 2 Duo 2.5GHz laptop.

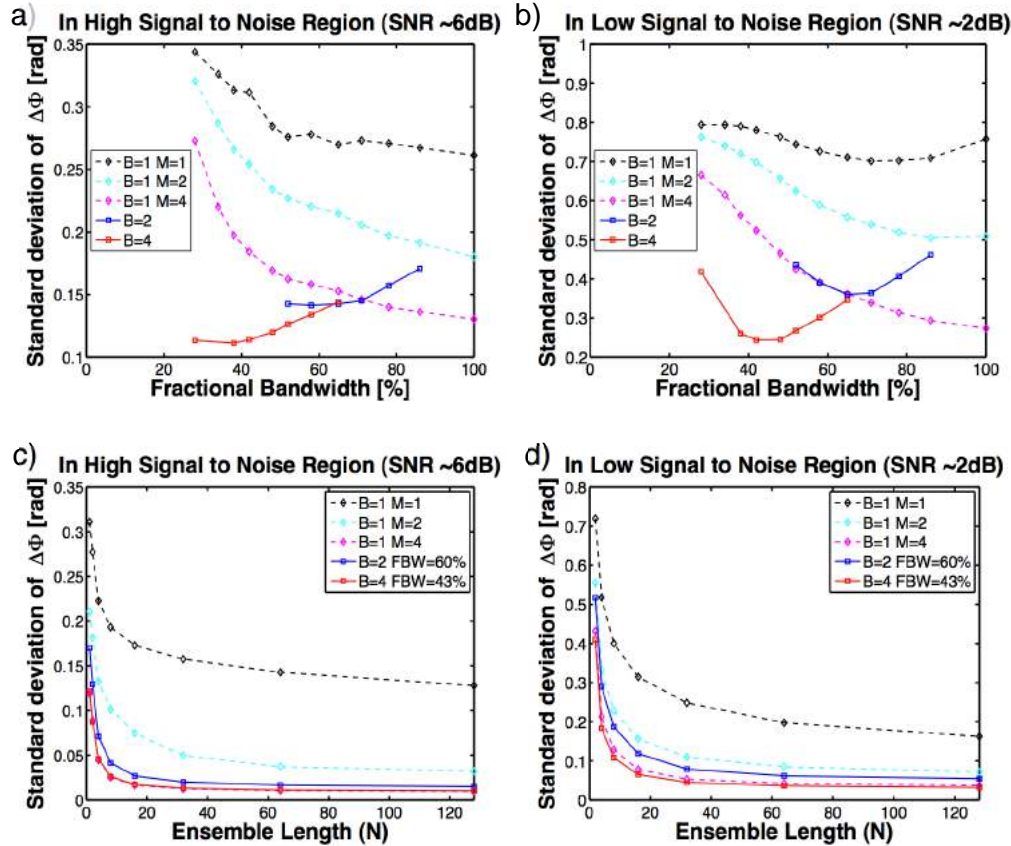


Fig. 3. A series of 20 structural OCT images were taken in B-mode of a stationary tissue phantom. (a) and (b): mean measurements of background phase noise (standard deviation of $\Delta\Phi$) using DOCT and ssDOCT at different fractional bandwidth (FBW) for high SNR (approx. 6dB) region and low SNR (approx. 2dB) region at an ensemble length $N=10$. In all ssDOCT calculations, $M=1$. The catheter beam was then set at a static position and 20 structural OCT images were taken in M-mode. (c) and (d): mean measurements of background phase noise using DOCT and ssDOCT at various ensemble lengths (N) for high SNR region and low SNR region.

3. Results and Discussion

3.1. Background noise in Split Spectrum Doppler Optical Coherence Tomography

The key parameters that controlled the overall performance of ssDOCT were the bandwidth of each window band $FWHM_b$ and the amount of overlap between the windows. The term fractional bandwidth (FBW) was denoted as $FBW = FWHM_b / FWHM_{full} \%$, where it was the ratio between the full width half maximum (FWHM) of a single band ($FWHM_b$) and the FWHM of the full window $FWHM_{full}$.

The mean standard deviation of $\Delta\phi$ for 20 frames (interframe) with a Kasai autocorrelation window (Eq. (23)) of ensemble length $N=10$ (transverse direction) are shown in Figure 3(a) & Figure 3(b). Various numbers of window bands (B) and the percentage of FBW were observed and compared to the conventional Kasai windows averaged in the axial direction (M). Utilization of more bands ($B=2$ & 4) resulted in lower background phase noise, as seen in Figure

3.

In both high SNR and low SNR regions, there was a local minimum in the background phase noise as a result of ssDOCT. This local minimum in noise versus FBW was expected because the overlap between the band windows became greater and approached the single apodization window condition. The single apodization window condition consisted of a non-split interferogram leading to the utilization of the maximum resolution and spectral power. The occurrence of the local minima may have been related to the spectral power that was used to resolve the Doppler signal and its corresponding axial resolution. In the case of ssDOCT, Eq. (21) demonstrates that splitting the spectrum into narrower bands reduces the standard deviation of the velocity estimation. A side effect is the decreasing of the spectral power for flow velocity estimation. By averaging across each unique bands, higher velocity resolution could be achieved while most of the spectral power is recovered. However, to fully account for all the phase noise terms such as transverse motion, additive noise components, and Eq. (21) needs to be considered in conjunction with multiple previous works [10, 21, 29–31].

Further increase in background noise could have also been attributed to sparsely spaced bands, which led to very little overlap or no overlap producing uncorrelated signals. This resulted in a picket fence effect where the loss of information occurred between the filters bands. Thus, careful design of the FBW must be taken into account, particularly in low SNR regions as the local minima is more pronounced (Figure 3(b)). When optimal values of FBW and B are selected, the ssDOCT demonstrated a larger decrease in background noise for low SNR regions compared to high SNR regions and equivalent axial averaging.

When observing a moving scatterer crossing a beam, an adequate number of A-lines was required to sufficiently evaluate the pulse duration of the resulting moving scatterer. In the rotary catheter regime, large ensemble lengths (N) were difficult to achieve as there was a finite amount of beam overlap between each A-line scan. Beyond this beam overlap, each additional A-line scan became decorrelated, which led to poor velocity estimates. In Figure 3(c) and Figure 3(d), the catheter beam was held at a static position to observe a single point of the phantom and isolated the effect of ensemble length under different conditions. Various ensemble lengths were evaluated and compared between the traditional DOCT and ssDOCT.

After the application of ssDOCT, both B=2 and B=4 phase noise plateaued at N=32 and had a similar performance as M=4 (traditional DOCT), approaching the limit of system performance as compared to the common path interferometer benchmark ($\Delta\phi$ 0.01 rad). It was demonstrated that ssDOCT can provide comparable velocity resolution than DOCT when averaging over 2 bands relative to averaging over 4 pixels in the axial direction (M). By averaging over 2 bands rather than 4 pixels, the resolution is less degraded. Furthermore, shorter ensemble lengths were required, allowing for higher lateral resolution and lower beam overlap.

3.2. *Slow flow imaging in Split Spectrum Doppler Optical Coherence Tomography*

Velocity estimation from both ssDOCT (right column) and DOCT (left column) techniques were examined in Figure 4. The structural images of the phantom were evaluated using Eq. (24) in Figures 4(a) (standard OCT processing: B=1, M=2, N=10) and 4(b) (SSP-OCT processing: B=4, M=1, N=10). The corresponding phase shift images (Figure 4(c) & Figure 4(d)) clearly depict the effect of Doppler artefacts throughout the image. This phase shift artefact originated from the catheter sheath area. Compensation was performed by taking into account the phase shift from internal reflection [10] of the catheter sheath and subtracting it from the image [5, 15, 32]. In Figure 4(e) & Figure 4(f), the low SNR regions (1.7mm to 2mm from the catheter) had less phase noise in ssDOCT than in DOCT.

To quantify the phase variation, the DOCT and ssDOCT velocity profiles for the vessel were generated using an averaging filter with a 32 x 32 kernel. This averaged profile was subtracted

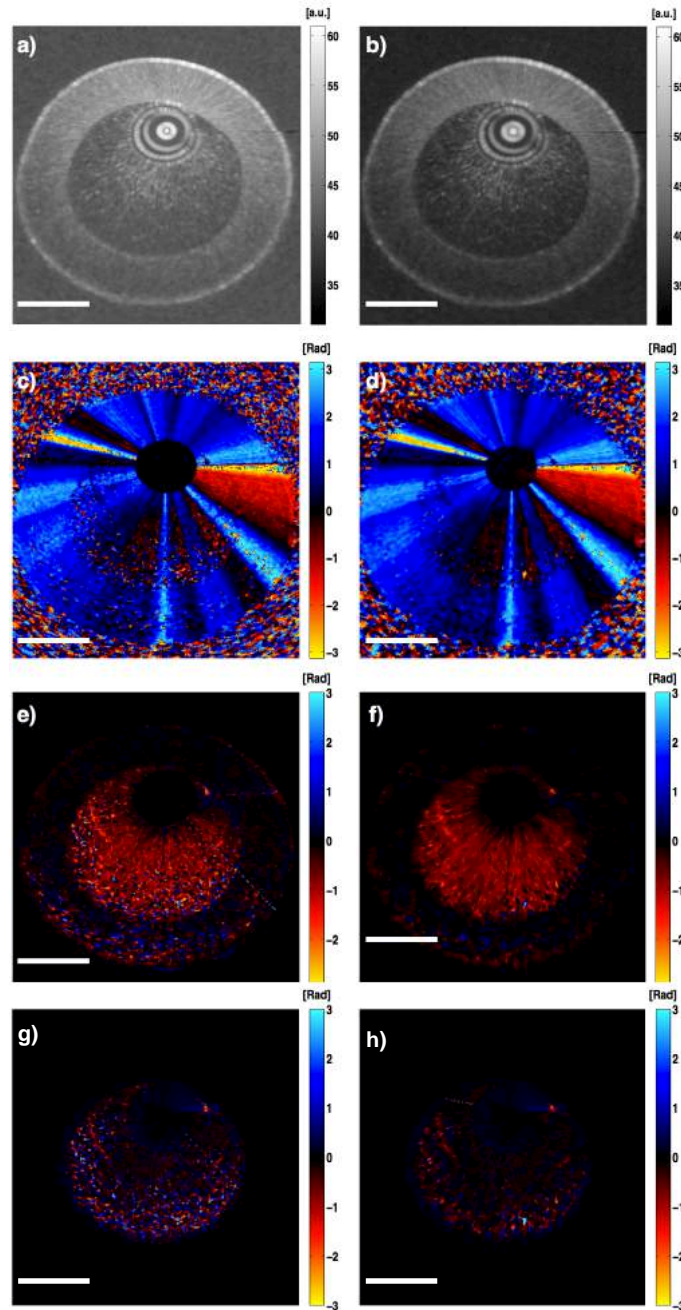


Fig. 4. (a) Structural image of a slow flow phantom with 1.5% diluted blood mixture realized using the full length apodization window ($B=1$, $M=2$, $N=10$). (b) The corresponding structural SSP-OCT image ($B=4$, $M=1$, $N=10$). (c) and (d) The Doppler shift of the slow flow phantom evaluated by DOCT and ssDOCT, respectively. Doppler artefacts were present in both images. (e) and (f) The corrected Doppler image computed from DOCT and ssDOCT techniques, respectively. The relative phase from (g) DOCT and (h) ssDOCT were then visualized by subtracting the averaged velocity profile. More phase noise is present in DOCT compared to ssDOCT. Scale bar = 1mm.

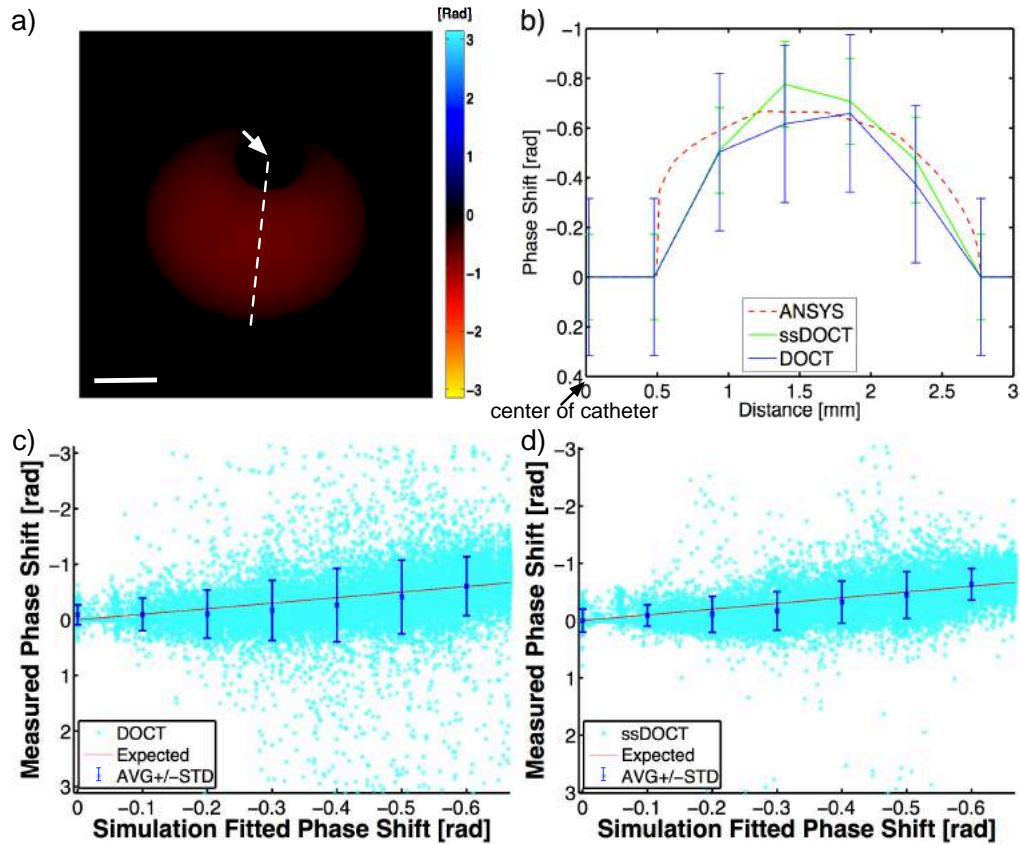


Fig. 5. (a) An ANSYS simulation fitted phase shift model of Figure 4 was generated. Scale = 1mm (b) The axial profile was taken (dashed line in (a)) from the center of the catheter (arrow) and the mean & standard deviation were compared. The expected velocity profile was then plotted against the measured phase shift of (c) DOCT (B=1, M=2, FBW=100%) and (d) ssDOCT (B=4, M=1, FBW=44%). The expected phase shift (red) and mean & standard deviation (blue) were plotted.

from the DOCT (Figure 4(g)) and ssDOCT (Figure 4(h)) images and resulted in the relative phase variation. The ssDOCT techniques showed a lower overall Doppler background noise within the flow regions ($RMS = 0.994$ rad) compared to the conventional DOCT ($RMS = 1.428$ rad).

This lowered Doppler background noise from the ssDOCT technique can further be seen in Figure 5. An ANSYS simulation fitted phase shift model (Figure 5(a)) was constructed based on the dimensions of the flow phantom. Taking a single axial scan (white dashed line) from the center of the catheter, it can be seen that the standard deviation are nearly half the value on the whole 3mm axial scan in ssDOCT compared to DOCT (Figure 5(b)). The entire ANSYS simulation fitted phase shift model were then plotted against the measured phase shift for both DOCT (Figure 5(c)) and ssDOCT (Figure 5(d)). The comparison of the previous DOCT assessment of the measured velocity versus phase shift in Part I of our companion papers [15] (a nearly ideal case) and the rotary catheter showed that the effects of the rotary catheter were more severe and inherently noisy. By utilizing ssDOCT, it was seen that the standard deviation (Figure 5(b)) is nearly half throughout various velocities compared to DOCT (Figure 5(a)).

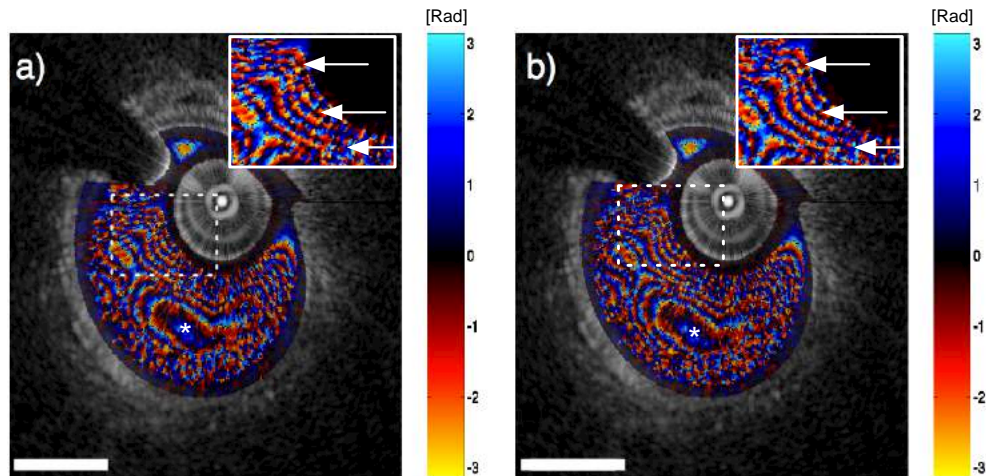


Fig. 6. The structural OCT image overlapped with Doppler image of a high flow region in a porcine carotid artery. (a) Doppler images produced by DOCT (B=1, M=4, FBW=100%). (b) The corresponding ssDOCT (B=2, M=1, FBW=60%) with approximately similar phase noise performance as shown in Figure 3(a). The arrows indicate less degradation in the visualization of the aliasing rings comparing (b) to (a). The unwrapped value in both DOCT and ssDOCT showed a peak velocity of 18.7π (asterisk). Scale bar = 1 mm.

Furthermore there is a significant reduction in the outlier data points. At lower velocity estimates (< -0.1 rad) the clustering of ssDOCT becomes tighter relative to DOCT suggesting that ssDOCT has the ability to detect lower velocities.

3.3. *In-vivo high flow imaging in Split Spectrum Doppler Optical Coherence Tomography*

The performance of ssDOCT in a high flow situation was evaluated in the porcine carotid artery (Figure 6) using the previously described imaging procedure [2, 5]. Due to the high flow velocities in the carotid artery, aliasing between $-\pi$ to π occurred, and produced contours in the form of rings. A comparative assessment of these aliasing rings suggested that the fine contours (arrow) were distinguished better in ssDOCT than DOCT techniques. The fine aliasing ring contours in DOCT appeared to be lost in the phase image, suggesting that axial resolution was not sufficient. The differentiation between the rings is critical for estimating the velocity. Any degradation between the rings would also degrade the velocity estimate. As a result, the utilization of B=2 with FBW of 60% demonstrates high velocity resolution while consisting of similar phase noise as traditional DOCT at M=4 (Figure 3). In both cases, the peak velocity was measured to be 18.7 rad (after unwrapping). Considering the minimum measurable phase shift is 0.2 rad, the dynamic range of velocity measurement demonstrated in this experiment is over 49 dB.

3.4. *In-vivo slow flow imaging in Split Spectrum Doppler Optical Coherence Tomography*

3.4.1. Flow pattern near stent struts in the carotid artery

The blood flow profile in stents plays an important role in its design and application. When the stent strut is placed onto the lumen wall, a flow dynamic phenomenon known as backward facing step flow or forward facing step flow occurs [33]. Under these flow conditions; a small region between the lumen and strut creates a separation zone where fluid does not mix with

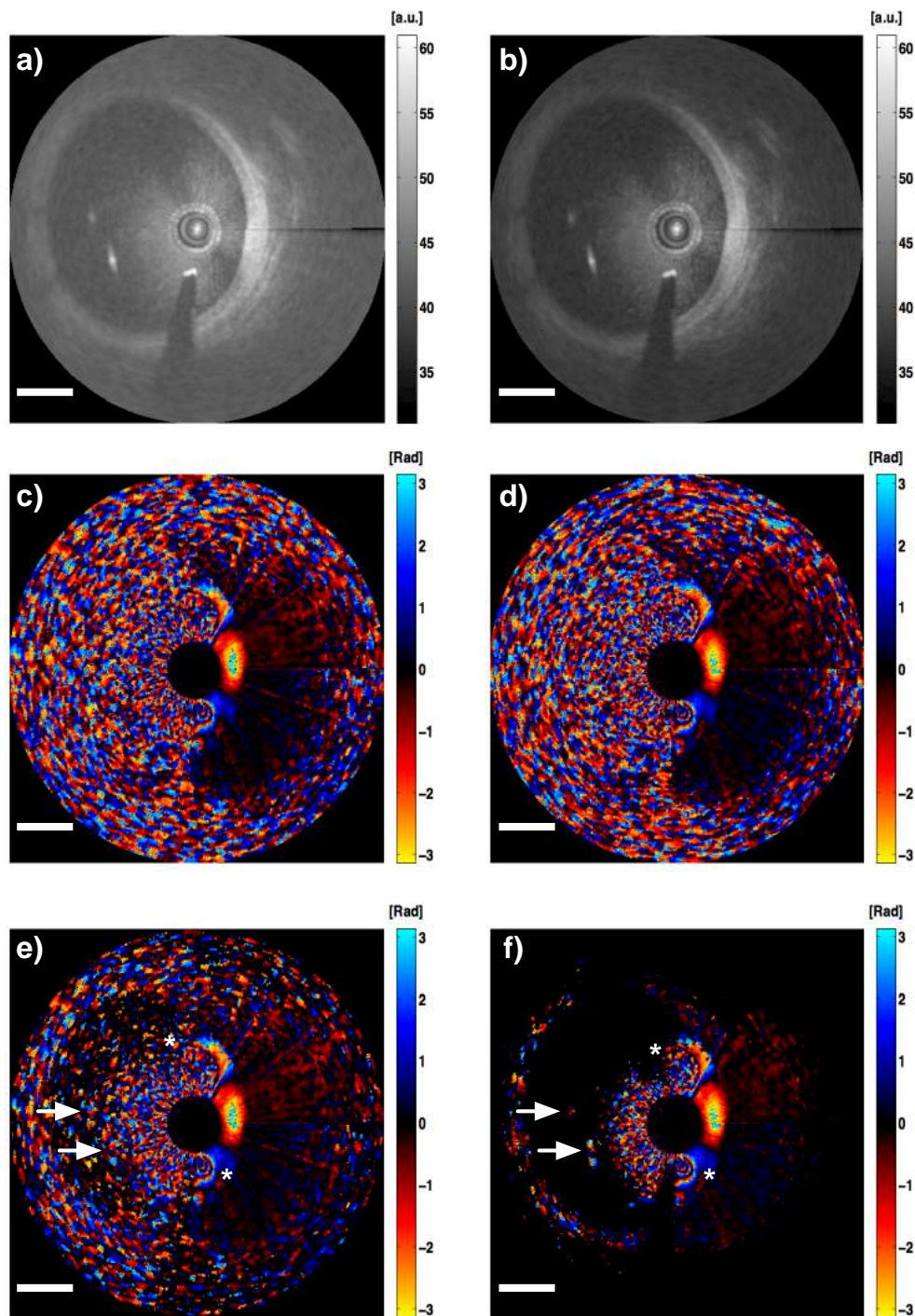


Fig. 7. (a) Structural image of a deployed stent in the carotid artery using the full length apodization window ($B=1$, $M=4$, $N=20$). (b) The corresponding structural SSP-OCT image ($B=2$, $M=1$, $N=20$, $FBW=60\%$). (c) and (d) The corrected Doppler image computed from DOCT and ssDOCT techniques, respectively. (e) DOCT and (f) ssDOCT were thresholded at the same phase value. Note the two detected flow profiles (upper * & lower *). The upper flow profile (*) may be caused from a stent strut upstream from the location of the OCT catheter imaging plane. The arrows denote the Doppler signal from the remaining two stent struts. Scale bar = 1mm.

the fluid in the mainstream [34]. This could result in the accumulation of thrombi and create other complications including injury to the smooth muscle cells, endothelial denudation, and disrupt the elastic laminae [34]. As a result, understanding the stent flow profiles could lead to improved stent designs and minimize complications.

The effects of blood flow profiles in stents have been demonstrated through mathematical flow dynamic models and have been measured in flow chambers using Doppler ultrasound, laser Doppler anemometry, and particle imaging velocimetry [34]. Based on clinical practice in carotid angioplasty and stenting, the un-apositioned stent strut may account for a significant area of total stent coverage, especially at the carotid bifurcation. To our knowledge, this paper is the first to directly visualize *in-vivo* flow patterns around stent struts using OCT with its inherent high spatial resolution and preserved by ssDOCT processing. Figures 7(a) & 7(b) shows the structural image of a deployed stent in the carotid artery using traditional OCT and split spectrum OCT, respectively. The corresponding bulk motion compensated Doppler image using traditional DOCT with $M=4$ and $N=20$ (Figure 7(c)) and ssDOCT with $B=2$, $N=20$, and $FBW=60\%$ (Figure 7(d)) are shown. The same phase thresholded value was utilized in DOCT (Figure 7(e)) and ssDOCT (Figure 7(f)). Overall, it was observed that the ssDOCT technique suppressed a significant amount of background phase noise with respect to DOCT. In both techniques, a flow profile adjacent to one of the stent strut (lower *) was observed and believed to be an eddy current from that strut. Closer observation of the flow profile revealed aliasing contours that were defined in ssDOCT compared to DOCT and suggested a higher velocity resolution. This was also perceived in a second detected eddy current (upper *) which may be caused from a stent strut upstream from the location of the OCT catheter. In terms of the other two stent struts (arrows), ssDOCT resolved the weak Doppler signal exhibited from them and separated it from the background noise.

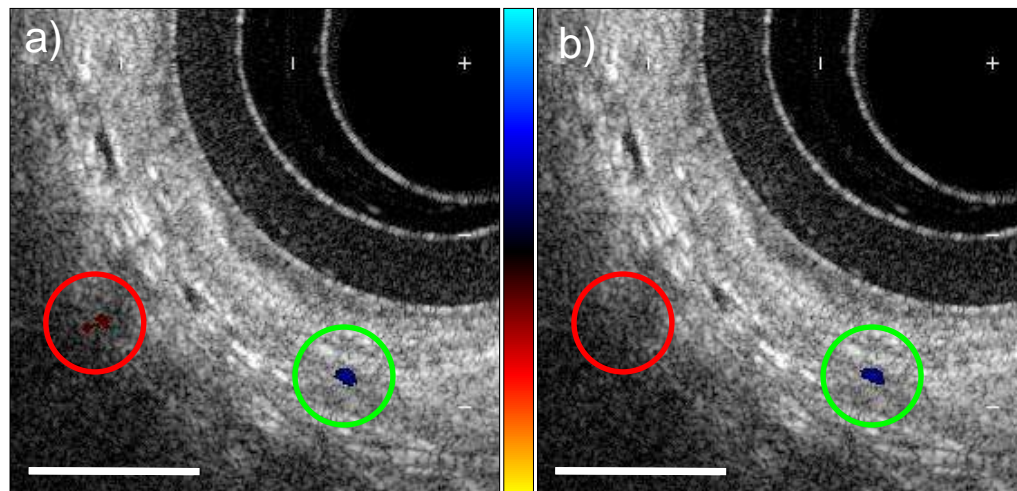


Fig. 8. (OCT imaging from an *in-vivo* human airway. (a) Structural OCT image with DOCT overlay ($B=1$, $M=8$, $N=32$). (b) Split spectrum processing ($B=4$, $M=2$, $N=32$, $FBW=60\%$) of the same imaging frame. Both images have identical Doppler display thresholds. The green circle indicates a true blood vessel confirmed by continuity between imaging frames. The red circle shows a Doppler artefact that was suppressed in the split spectrum processed image. The color-coded CDOCT scale bar spans ± 8.5 mm/s. Scale bar = 0.5mm.

3.4.2. Human Airways

The utility of ssDOCT for low velocity imaging was also demonstrated in the human lung. Conventional DOCT vasculature imaging in human airways using rotary probes requires phase thresholding and large Kasai autocorrelation windows [4] to decrease the Doppler artefacts. Figure 8 shows the same structural OCT image from a human airway with DOCT ($B=1$, $M=8$, $N=32$) overlay (Figure 8(a)) and ssDOCT ($B=4$, $M=2$, $N=32$, $FBW=60\%$) overlay (Figure 8(b)) using the same Doppler phase threshold as DOCT. The Doppler signal indicated by the green circle shows a blood vessel confirmed by observing the same feature in adjacent frames of a pullback. The Doppler signal within the red circle was only visible in the DOCT overlay and is a Doppler artefact. To remove this artefact from the DOCT overlay, the Doppler phase threshold would need to be raised to eliminate more low flow velocities. The raised Doppler phase threshold can have drawbacks as it could eliminate true low flow velocities providing a false-negative. Thus, ssDOCT provided more specific detection of low vascular velocity.

4. Conclusion

We have demonstrated a new method of Doppler OCT imaging, which consisted of splitting the OCT spectral interferograms into multiple bands. A theoretical model was developed which demonstrated a decrease in standard deviation of phase shift as the spectral bandwidth decreased. The number of bands (B) and fractional bandwidth of each of the band (relating to the width of the band and the overlap) were investigated. ssDOCT was demonstrated to have greater sensitivity in velocity estimation and may be useful for measuring smaller blood vessels or weak Doppler signals from stent struts in OCT rotary catheter imaging. The ssDOCT can outperform DOCT without sacrificing resolution from large axial averaging windows. This work also showed the first *in-vivo* stent flow profile, where the Doppler images benefited from the utilization of ssDOCT. Adaptive ssDOCT could be deployed based on the SNR of the OCT image in the future. This would reduce the computational time in a real-time implementation and could enhance the current Doppler algorithm.

Acknowledgments

The authors acknowledge Danielle Gifford, Adrian Mariampillai, Kyle H. Y. Cheng, Kenneth K.C.Lee, and Beau A. Standish for their technical assistance and helpful discussions. This work was supported by the Canadian Institutes of Health Research, the Natural Sciences and Engineering Research Council of Canada, the Ontario Brain Institute, Ryerson University, the Canada Research Chair Program, and the Canada Foundation for Innovation.